Synergistic enhancement of immunological responses triggered by hyperthermia sensitive Pt NPs *via* NIR laser to inhibit cancer relapse and metastasis

Jie Yu [a,b], Sha Liu [a], Yupeng Wang [a], Xidong He [a,b], Qingfei Zhang [a], Yanxin Qi [a,*], Dongfang Zhou [a], Zhigang Xie [a,b], Xiaoyuan Li [a,c,**], Yubin Huang [a,c,***]

[a] *State Key Laboratory of Polymer Physics and Chemistry, Changchun Institute of Applied Chemistry, Chinese Academy of Sciences, Changchun, 130022, PR China*
[b] *University of Science and Technology of China, Hefei, 230026, PR China*
[c] *Faculty of Chemistry, Northeast Normal University, Changchun, 130024, PR China*

ARTICLE INFO

ABSTRACT

The combination of tumor ablation and immunotherapy is a promising strategy against tumor relapse and metastasis. Photothermal therapy (PTT) triggers the release of tumor-specific antigens and damage associated molecular patterns (DAMPs) in-situ. However, the immunosuppressive tumor microenvironment restrains the activity of the effector immune cells. Therefore, systematic immunomodulation is critical to stimulate the tumor microenvironment and augment the anti-tumor therapeutic effect. To this end, polyethylene glycol (PEG)-stabilized platinum (Pt) nanoparticles (Pt NPs) conjugated with a PD-L1 inhibitor (BMS-1) through a thermosensitive linkage were constructed. Upon near-infrared (NIR) exposure, BMS-1 was released and maleimide (Mal) was exposed on the surface of Pt NPs, which captured the antigens released from the ablated tumor cells, resulting in the enhanced antigen internalization and presentation. In addition, the Pt NPs acted as immune adjuvants by stimulating dendritic cells (DCs) maturation. Furthermore, BMS-1 relieved T cell exhaustion and induced the infiltration of effector T cells into the tumor tissues. Thus, Pt NPs can ablate tumors through PTT, and augment the anti-tumor immune response through enhanced antigen presentation and T cells infiltration, thereby preventing tumor relapse and metastasis.

1. Introduction

Radiotherapy, chemical and biological ablation, photodynamic therapy (PDT) [1], cryoablation, photothermal therapy (PTT) and electric or microwave-based ablation [2–4] are minimally invasive strategies for treating unresectable local tumors [5,6]. PTT triggers cancer cell death and destruction of the tumor microvasculature through hyperthermia following exposure to near-infrared (NIR) light. In fact, the necrotic and apoptotic tumor cells remaining after PTT release antigens that may elicit a tumor-specific immune response [7–9] and facilitate the production of pro-inflammatory factors [10,11], although

this response is not sufficient to eliminate the residual malignant cells [12–15]. Therefore, it is necessary to combine tumor ablation with systematic immunomodulation to augment the tumor-specific immune response [16–18].

Platinum nanoparticles (Pt NPs) [19] are selectively toxic against cancer cells [20–24] and undergo photothermal conversion through non-radiative relaxation [25] under near-infrared resonance (NIR) exposure [26], resulting in targeted hyperthermia [27–30] and antigen-release [31,32]. In addition, ultra-small NPs also act as adjuvants [33] to stimulate dendritic cells (DCs) maturation [34,35]. Adequate antigen presentation [36] is crucial for eliciting a

tumor-specific immune response [37,38]. Therefore, it is vital to facilitate antigen recognition and antigen presentation in order to optimize stimulation of effector immune cells. Antigens captured by Maleimide (Mal)-modified nanoparticles (NPs) would form the in-situ vaccines, resulting in improved antigen presentation [39,40]. However, since Mal is highly sensitive to most proteins, Mal-modified NPs can potentially bind to non-antigenic proteins as well [41]. Therefore, shielding the Mal moiety before antigen exposure may improve antigen capture efficiency. Finally, the DCs subsequently activated by the Pt NPs would present the processed antigens to T cells after internalizing cellular debris containing tumor-associated antigens, thereby triggering an immune response [42].

While PTT eliminates most tumor cells, those remaining can induce an immunotolerant microenvironment [43,44], which severely limits the efficacy of anti-cancer immunotherapies [45–47]. For example, tumors escape immune elimination by upregulating PD-L1, which then binds to the inhibitory receptor PD-1 on tumor-specific T cells and restrains T cell activation and proliferation [48,49]. Thus, PD-1/PD-L1 checkpoint blockade [50] alleviates T-cell exhaustion and induces the infiltration of activated T cells [51]. The PD-L1 small molecule inhibitor (BMS-1) offers several advantages over therapeutic antibodies in the context of immune checkpoint blockade (ICB) therapy, such as lower production costs, higher stability, improved tumor penetration and low immunogenicity [52–54]. In addition, BMS-1 can be easily modified with a furan functional group, which can shield Mal through a Diels-Alder reaction before antigen release. Furthermore, the retro-Diels-Alder reaction in response to the heat generated by

photothermal conversion can reverse Mal protection by releasing BMS-1 [55–57].

Therefore, combining Pt NPs with BMS-1 in a smart response system is a promising strategy against cancer relapse and metastases. In this study, we conjugated BMS-1 with Mal-modified PEG *via* thermo-sensitive Diels-Alder reaction, and synthesized I-Pt NPs with BMS-1 conjugated PEG as the capping agents to improve biocompatibility and functionality (Scheme 1). In response to NIR laser irradiation, the I-Pt NPs undergo photothermal conversion and trigger PTT mediated tumor ablation. The ensuing hyperthermia releases BMS-1 and uncaps Mal. Tumor-associated antigens released from the cellular debris are then captured by the exposed Mal through the sulfhydryl groups on proteins and presented by the APCs [39]. In the presence of tumor antigens released from the necrotizing cells in-situ [58], the Mal-Pt NPs exhibit vaccine-like [59,60] properties (triggering DCs maturation and capturing antigens) and recruit DCs into the tumor microenvironment [61]. Finally, the BMS-1 released in response to hyperthermia relieves the immunosuppressive tumor microenvironment and further augments the immune response. The stimuli-responsive exposure of Mal groups on the NPs avoids non-specific binding and improves the efficiency of antigen-capturing. Taken together, this novel nano-system can synergistically augment immunological responses and photothermally ablate tumors. Therefore, a systematic immunomodulation immunotherapy that synergizes antigen exposure, antigen capture, and T cell activation can augment the anti-tumor immune responses [62] and prevent cancer relapse and metastasis [63–66].
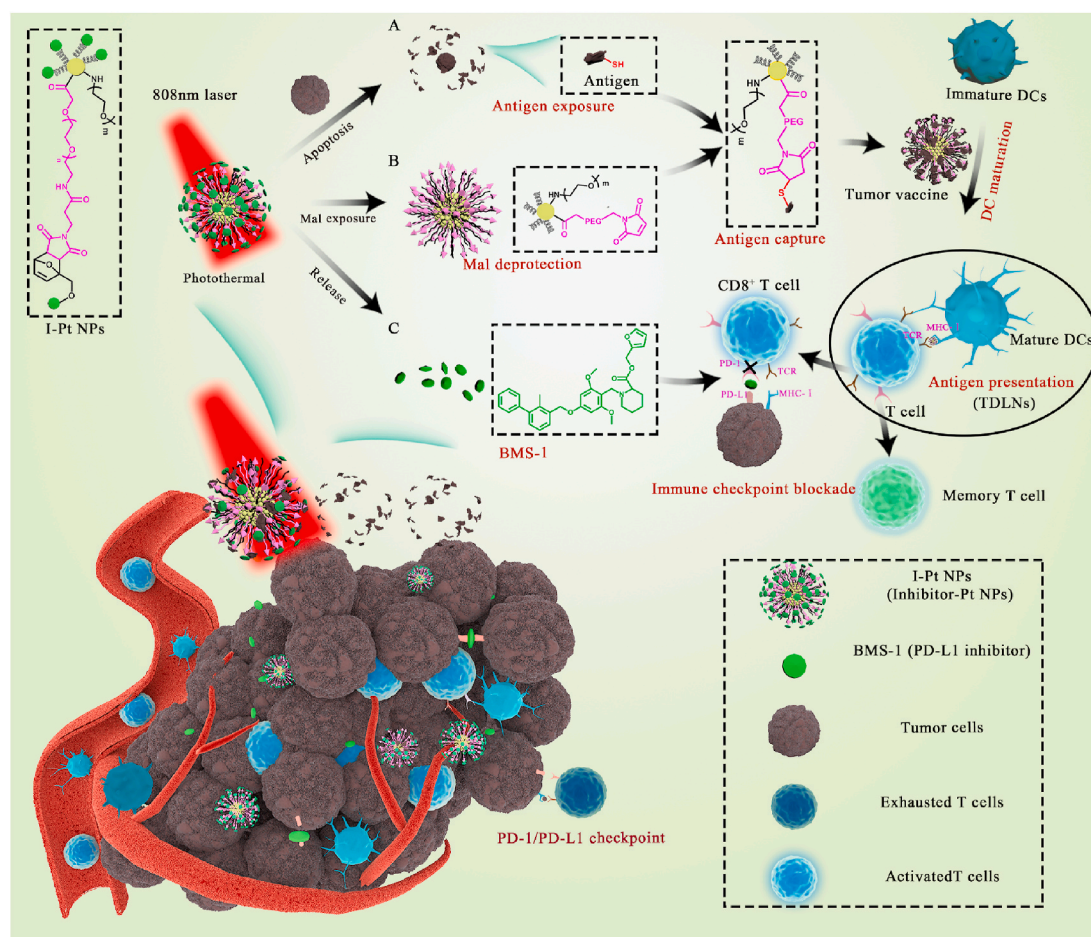
Scheme 1. Schematic illustration of Pt NPs conjugated with BMS-1 through hyperthermia-sensitive linkage for NIR-controlled release of inhibitor and exposure of Mal. A thermal-sensitive release and Mal deprotection procedure is achieved by the Retro D-A reaction. Exposed Mal on the surface of Pt NPs captures the antigens from ablated tumor cells and promotes antigen presentation. The released BMS-1 alleviates T cell exhaustion and induces infiltration of effector T cells.

2. Materials and methods

2.1. Materials

K$_2$PtCl$_4$ was bought from Shandong Boyuan Chemical Company, China. N,N′-Dicyclohexylcarbodiimide (DCC), 4-dimethylaminopyridine (DMAP), furfuryl alcohol, Rhodamine B (RhB) and NaBH$_4$ were purchased from Aladdin. Maleimide-PEG$_{2k}$-COOH (Mal-PEG$_{2k}$-COOH) and PD-L1 inhibitor (BMS-1) were purchased from Xi'an ruixi Biological Technology Co., Ltd, China. mPEG$_{2k}$-OH was purchased from Sigma-Aldrich. Fetal bovine serum (FBS), Dulbecco's modified eagle medium (DMEM) and Roswell Park Memorial Institute 1640 (RPMI-1640) were purchased from Thermo-Fisher. OVA was purchased from InvivoGen. 3-(4,5-dimethylthiazol-2-yl)-2,5-diphenyltetrazolium bromide (MTT) and Hoechst 33258 were bought from Sigma-Aldrich. Granulocyte-macrophage colony stimulating factor (GM-CSF), interleukin-4 (IL-4), Lipopolysaccharide (LPS), enhanced bicinchoninic acid (BCA) protein assay kit, hematoxylin and eosin (H&E) were purchased from Beijing Solarbio Science & Technology Co., Ltd. The DeadEnd™ fluorometric TUNEL system for apoptosis detection was purchased from Promega Corporation, USA. Enzyme linked immunosorbent assay (ELISA) kits were purchased from Lengton Biotechnology, China. Anti-CD80/FITC, Anti-CD86/APC and Anti-CD11c/PE-Cy7 were purchased from Bioss Biotechnology Co., Ltd., Beijing, China. FITC anti-mouse CD3 Antibody, APC anti-mouse CD8a Antibody, APC anti-mouse CD4 Antibody, PE anti-mouse CD25 Antibody, PE anti-mouse CD44 Antibody, PE-Cy5.5 anti-mouse CD62L Antibody and anti-mouse CD16/32 were purchased from Biolegend.

2.2. Modification of PEG

RhB (100 mg, 208 nmol), furfuryl alcohol (81.83 mg, 832 nmol), DCC (64.60 mg, 313 nmol) and DMAP (12.73 mg, 104 nmol) were added to the anhydrous polymerization bottle and resolved with anhydrous CH$_2$Cl$_2$ (10 mL). The reaction was kept at room temperature for 3 days. A drop of water was added to terminate the reaction and DCC was converted to DCU which was removed by freezing filtration. Furfuryl RhB was obtained by settling with cold ether and filtration. The obtained Furfuryl RhB was characterized by ^{1}H NMR and ESI-MS. Furfuryl BMS-1 was obtained according to the same process.

Mal-PEG$_{2k}$-COOH (50 mg, 25 nmol) and furfuryl RhB (109 mg, 210 nmol) were mixed and dissolved in anhydrous CH$_2$Cl$_2$ (10 mL). The reaction was kept at room temperature for 7 days. After rotary evaporation, the product was dissolved in H$_2$O and dialyzed for 3 days to remove the unreacted furfuryl RhB. The obtained RhB-PEG$_{2k}$-COOH (R-PEG$_{2k}$-COOH) was characterized by ^{1}H NMR. Conjugation of Mal-PEG-COOH (50 mg, 25 nmol) with furfuryl BMS-1 (116 mg, 210 nmol) was operated in similar procedures to obtain BMS-1-PEG$_{2k}$-COOH (I-PEG$_{2k}$-COOH).

2.3. Synthesis of M-Pt NPs (mPEG$_{2k}$-COOH capped Pt NPs), R-Pt NPs (R-PEG$_{2k}$-COOH capped Pt NPs) and I-Pt NPs (I-PEG$_{2k}$-COOH capped Pt NPs)

K$_2$PtCl$_4$ (20 mg, 48.2 nmol), mPEG$_{2k}$-NH$_2$ (50 mg, 25 nmol) and mPEG$_{2k}$-COOH (100 mg, 50 nmol) were dissolved in H$_2$O, and stirred for 4–8 h NaBH$_4$ dissolved in H$_2$O was added to the reaction system and stirred for another 4 h at 25 °C. The resulted Pt NPs were dialyzed against water for 3 days to remove the redundant NaBH$_4$. R-Pt NPs or I-Pt NPs were synthesized through the same procedure by replacing mPEG$_{2k}$-COOH with R-PEG$_{2k}$-COOH or I-PEG$_{2k}$-COOH.

2.4. Photothermal responses of Pt NPs

Pt NPs were irradiated with an 808 nm laser at intensity of 0.8 W/cm^2 for 10 min and deionized water was measured as a control. Different Pt NPs concentrations and laser intensity were applied to determine the optimal photothermal activity. Various concentrations (1.32, 0.66, 0.3, 0.22, 0.16, 0.08 mM) of Pt NPs in individual 96-well plates were irradiated with the 808 nm laser at different power density of 0.8 W/cm^2 for 10 min. Pt NPs (0.22 mM, 200 μL) were irradiated with 808 nm laser at different power densities (0.50, 0.75, 1.00, 1.25, 1.50 W/cm^2) for 10 min. Temperature changes of the solution were monitored by a thermocouple probe. Thermocouple probe and the laser path were kept in a parallel direction. Secure digital (SD) card was used to record the data every 10 s.

2.5. Triggered release of RhB and BMS-1

R-Pt NPs in 24-well plates (0.22 mM) were irradiated with the 808 nm (0.8 W/cm^2) laser for different time (0 s, 30 s, 60 s, 2 min, 3 min, 4 min, 5 min). And then fluorescence images of the solution were acquired at predetermined time (excitation wavelength, 488 nm; emission wavelength, 515 nm). Afterwards, the solution was diluted in tenfold and the fluorescence spectrum was measured (excitation wavelength, 520 nm; emission wavelength, 550–700 nm).

I-Pt NPs in 24-well plates (0.22 mM) were irradiated with 808 nm laser (0.8 W/cm^2) for different time and the released BMS-1 was collected by the ultrafiltration tube (3000 Da, 3000 r/min, 15 min). Analytical HPLC was carried out to quantify the released BMS-1 with a UV/Vis variable wavelength detector, on an AQ C18 column at 25 °C and at 0.8 mL min^{-1} with CH$_3$OH: H$_2$O = 3:1. All chromatograms were recorded at λ = 214 nm.

2.6. Cell lines and animals

Mouse breast cancer 4T1 was bought from Institute of Biochemistry and Cell Biology, Chinese Academy of Sciences, and cultured with DMEM (10% fetal bovine serum; 5% CO$_2$ at 37 °C). DC 2.4 was purchased from Fenghui Biological Technology Co., Ltd, China, and cultured with 1640 (10% fetal bovine serum; 5% CO$_2$ at 37 °C). Bone marrow-derived DCs (BMDCs) were extracted from the femur and tibia bones of Balb/c and cultured in 10 mL RPMI 1640 medium containing 10% FBS, 10 ng/mL GM-CSF and 5 ng/mL IL-4. (5% CO$_2$ at 37 °C) [58] Female Balb/c mice (6–8 weeks) were bought from Liaoning Changsheng Biotechnology Co., Ltd., China. All animal experiments have been approved and carried out according to the guidelines of Changchun Institute of Applied Chemistry Studies Committee, Chinese Academy of Sciences.

2.7. Antigen-capturing of Pt NPs

Pt NPs, R-Pt NPs, I-Pt NPs (1 mM, 200 μL) in individual 96-well plates were irradiated with the 808 nm laser (0.8 W/cm^2) for 5 min. Irradiated Pt NPs were diluted 10 times and the released RhB or BMS-1 was removed and washed with the ultrafiltration tube (3000 Da, 3000 r/min, 15 min). The remained Pt NPs were incubated with OVA for 24 h at 37 °C. Excess OVA was removed and washed with the ultrafiltration tube (100 kDa, 3000 r/min, 15 min) for at least 5 times. Diameter and Zeta potential of Pt NPs after incubation with OVA were tested.

4T1 cells were seeded at a concentration of 5000 cells/well into 96-well plates and incubated overnight at 37 °C. Then 100 μL of M-Pt NPs, R-Pt NPs, I-Pt NPs were added to the well at a final concentration of 1 mM and cultured for 24 h. All the groups were irradiated with 808 nm laser (0.8 W/cm^2) for 5 min and then incubated for another 24 h. The residual NPs were isolated and excess H$_2$O$_2$ was added to destroy the NPs and remove the influence of Pt NPs on the BCA kit. Subsequently, the captured protein was quantified with BCA kit [41].

2.8. Cellular uptake of Pt NPs and OVA-Pt NPs

5×10^5 4T1 and DC2.4 cells were incubated in 6-well plates

overnight respectively. Pt NPs were added to the well at a final concentration of 50 μM and incubated for 1 h, 6 h and 12 h at 37 °C. Cell samples were washed with ice-cold PBS three times and counted before testing. Concentrated nitric acid, H_2O_2 and water were added sequentially to decompose organic substances in the cells and Pt concentration was determined with ICP.

OVA (20 mg) was dissolved in sodium carbonate buffer (10 mL, pH 9.8, 25 mM) and then mixed with FITC (400 μL, 1 mg/mL) at 4 °C overnight under stirring. The mixtures were dialyzed (MWCO = 7000 Da) against water for 2 days. After that, the purified solution was lyophilized to obtain OVA-FITC.

R-Pt NPs and I-Pt NPs (1 mM, 1 mL) were irradiated with 808 nm laser (0.8 W/cm^2). Released RhB or BMS-1 was removed and washed with the ultrafiltration tube (3000 Da, 3000 r/min, 15 min). FITC-OVA (1 mL) was added to the Mal exposed I-Pt NPs (+), R-Pt NPs (+), or M-Pt NPs (+) and incubated for 24 h at 37 °C in dark. Excess FITC-OVA was washed with the ultrafiltration tube (100 kDa, 3000 r/min, 15 min). Bone marrow-derived DCs (BMDCs) extracted from the femur of Balb/c were incubated with FITC-OVA-Mal-Pt NPs, FITC-OVA-M-Pt NPs, or FITC-OVA (quantified by UV absorption at 488 nm) for 24 h. Flow cytometry was then used to determine the uptake of FITC by BMDCs.

2.9. Cytotoxicity of Pt NPs

4T1 cells were cultured and irradiated in the same process as above and MTT was used to determine the cytotoxicity of Pt-NPs after irradiation. The standard MTT test was applied to measure the cell viabilities relative to untreated cells.

2.10. Pt NPs-based PTT induces DC maturation and stimulates the expression of pro-inflammatory cytokines in vitro

DC2.4 cells were seeded in 24-well plates and treated with Pt NPs (1 nM, 10 nM and 100 nM) or lipopolysaccharides (LPS) at 1 μg/mL. After incubating for 24 h, confocal fluorescence was used to visualize the maturation status of DC2.4 by staining FITC-CD80 (excitation: 488 nm).

In another transwell system, 4T1 cancer cells were seeded in the upper chamber and treated with Pt NPs, R-Pt NPs or I-Pt NPs (1 mM, 200 μL). NIR laser irradiation was applied to ablate these cells. Then this upper chamber was placed onto another lower chamber seeded with BMDCs. Micro pores (pore size 1 μm) between two chambers facilitate the diffusion of NPs and tumor antigen, so they can interact with BMDCs in the lower chamber. BMDCs were co-stained with CD11c (the specific marker of DCs), CD80 and CD86 (maturation markers) and analyzed with flow cytometry to determine the maturation content. Supernatants of BMDCs were collected and various factors such as IL-1β and IL-12p70 were analyzed with ELISA kits according to vendors' instructions.

2.11. Accumulation of Pt NPs in the nearest lymph nodes

Healthy mice were subcutaneously injected with Pt NPs. The nearest lymph nodes were isolated and weighted. Pt concentration was quantified with ICP as above. Mice were injected with FITC-OVA-Mal-Pt NPs, FITC-OVA-M-Pt NPs, or FITC-OVA and fluorescence images of the nearest lymph nodes were acquired 6 h later.

2.12. Pt NPs-based PTT induces DC maturation and stimulates the expression of pro-inflammatory cytokines in vivo

To investigate the adjuvant effect of Pt NPs *in vivo*, healthy mice were subcutaneously injected with Pt NPs at various doses. After 24 h, cells in the nearest lymph nodes were isolated and stained with PE-Cy7/CD11c (the specific marker of DCs), FITC/CD80 and APC/CD86 (the maturation marker of DCs) for flow cytometry measurement.

To investigate the maturation status of DCs after Pt NPs-based PTT *in vivo*, 4T1 tumor-bearing mice were injected with M-Pt NPs, R-Pt NPs, I-

Pt NPs (1.25 mg/kg) intratumorally. The tumor sites of the mice in the photo group were exposed to 808 nm laser with a power density of 0.8 W/cm^2 for 5 min. Mice were sacrificed at 12 h post injection of Pt NPs and the maturation status of DCs in the nearest lymph nodes was assessed using flow cytometry by co-staining with PE/Cy7-CD11c, FITC-CD80 and APC-CD86. Serum samples were isolated from mice after various treatments and diluted for analysis. IL-1β, TNF-α, IL-12p70 and IL-6 were analyzed with ELISA kits as above. All measurements were carried out in triplicate.

2.13. In vivo animal models

Remote memory model of Pt NPs-based photothermal therapy. For the first tumor inoculation, 4T1 cells (1×10^6) suspended in PBS were subcutaneously injected into the left flank mammary gland of each 6-week female Balb/c mouse to develop an orthotopic tumor model. For the second tumor inoculation, 4T1 cells (2×10^5) suspended in PBS were subcutaneously injected into the right flank of each female Balb/c mouse. Mice bearing 4T1 tumors received different treatment when their first tumor volumes reached 100–150 mm^3. Mice were randomly divided into six groups (n = 8), including: (1) Saline, (2) M-Pt NPs, (3) R-Pt NPs, (4) I-Pt NPs, (5) M-Pt NPs (+), (6) R-Pt NPs (+), (7) I-Pt NPs (+). For photothermal therapy of the first tumor, mice were intratumorally injected with Pt NPs (1.25 mg/kg). After injection, tumors were irradiated with NIR light (0.8 W/cm^2, 808 nm) for 5 min. IR thermal imaging was conducted by an IR thermal camera (Infrared Cameras. Inc.). The tumor volume was calculated every other day according to the following formula: (width^2 × length)/2. At the end of the experiment, mice were sacrificed and tumors were excised, weighed and photographed. Serum of each group of mice was collected for the testing of ELISA and other clinical chemical parameters. The tumors were harvested to produce a single-cell suspension according to the specified procedures. The harvested cells were further stained with several fluorochrome-conjugated antibodies: FITC-CD3, APC-CD4, PE-CD25 or FITC-CD3, APC-CD8.

Memory evaluation of Pt NPs-based photothermal therapy on a recurrence model. On Day −7, 4T1 cells (1×10^6) suspended in PBS were subcutaneously injected into the left flank mammary gland of each 6-week female Balb/c mouse to develop an orthotopic tumor model. On Day 1, mice were grouped and treated with photothermal therapy as same as the first tumor introduced as mentioned above. On Day 21, another small tumor was inoculated into the left leg by subcutaneously injecting 4×10^5 cell and calculated the tumor free rate for 2 weeks. The spleens were harvested to produce a single-cell suspension according to the specified procedures. The harvested cells were further stained with several fluorochrome-conjugated antibodies: FITC-CD3, APC-CD8, PE-CD44 and Percp/Cy5.5-CD62L.

Memory evaluation of Pt NPs-based photothermal therapy on a lung metastasis tumor model. On day −7, 4T1 cells were subcutaneously injected to develop an orthotopic tumor model as mentioned above. On Day −1, mice were challenged by i.v. injection of 4T1 tumor cells (1×10^5). On Day 1, mice were grouped and treated with photothermal therapy as above. For the control group, mice received surgery treatment to remove the primary subcutaneous tumors. On Day 58, animals were sacrificed for H&E staining. At the same time, the other mice were sacrificed right after being injected with India ink through the trachea. Lungs were then excised, bleached with Fekete's solution [67] for 10 min, followed by washing with Fekete's solution. Tumor metastasis sites subsequently appeared as white nodules on the surface of black lungs and were counted under a microscope.

2.14. Cytokine detection

Supernatants of BMDCs and serum samples were isolated from mice after various treatments and diluted for analysis. IL-12, IL-1β, IL-6 and TNF-α were analyzed with ELISA kits according to vendors instructions.

2.15. Analysis of immune cells after different treatment by flow sight

To study the immune cells in lymph nodes, tumors and spleen, single-cell suspensions were prepared according the existing protocol. Specifically, tissues were excised at the end of the study, and were transferred to a dish and cut into small pieces (less than 1 mm^3). The pieces were incubated in 1 mL of digestion solution (400 μg/mL type I collagenase and 100 μg/mL type IV collagenase in RPMI-1640 medium containing 10% FBS) and incubated at 37 °C for 2 h with persistent agitation. The suspensions were filtered by a 200-mesh sieve to remove the remained tissues and then collected the cells by centrifugation at 1,500 rpm for 10 min at 4 °C. The supernatant was discarded. 3–5 fold volume of Diluted Red Blood Cell Lysis Buffer was added and incubated for 1–2 min. And then cells were washed with PBS 7.4. Trion-100 was added to increase the permeability of the cells and facilitate the intracellular receptor staining if necessary. And then the cells were washed with PBS 7.4 and blocked the Fc-Receptors with anti-mouse CD16/32. Finally, cells were stained with fluorescence-labeled antibodies. For the analysis of the maturation status of DCs, DCs collected from lymph nodes were stained with PE/Cy7-CD11c, FITC-CD80, APC-CD86. DCs were CD11c$^+$ and maturation DCs were CD11c$^+$CD80$^+$CD86$^+$. For the analysis of the immune response at the tumor site, cells collected from the secondary tumor of the mice after various treatment were splited in half and stained with antibodies cocktails of FITC-CD3, APC-CD8 or FITC-CD3, APC-CD4, PE-CD25 respectively. Cytotoxic T lymphocytes (CTL) and helper T cells were CD3$^+$CD8$^+$ and CD3$^+$CD4$^+$, respectively. CD4$^+$ helper T cells were classified into effective T cells (CD3$^+$CD4$^+$CD25$^-$) and regulatory T cells (Tregs) (CD3$^+$CD4$^+$CD25$^+$). For analysis of memory T cells, spleen harvested from mice after various treatment were extracted a sing-cell suspension and stained with antibodies of FITC-CD3, APC-CD8, PE-CD44 and Percp/Cy5.5-CD62L according to the manufacturer. Central memory T cells (T$_{CM}$) and effector memory T cells (T$_{EM}$) were CD3$^+$CD8$^+$CD62L$^+$CD44$^+$ and CD3$^+$CD8$^+$CD62L$^-$CD44$^+$, respectively.

2.16. Immunohistochemistry (IHC)

At the end of tumor inhibition study, mice were sacrificed. Lung and tumor were excised and collected, fixed with 4% neutral buffered paraformaldehyde, embedded in paraffin, and then the tissues were cut into slices of 2 μm thick using microtome YD-1508A and mounted onto glass slides. For histological analysis, all the tissues were stained with H&E and visualized by BioTek Cytation™ 5. The aforementioned sliced tumor tissue sections were used for *in situ* nick-end labelling of nuclear DNA fragmentation with a TUNEL apoptosis detection kit according to the supplier's instructions and analyzed by BioTek Cytation™ 5.

2.17. Statistical analysis

Data were expressed as mean ± SD. The one-way ANOVA analysis was used to determine the statistical significance using no significance: n.s., *$P < 0.05$, **$P < 0.01$, ***$P < 0.001$.

3. Results and discussion

3.1. Preparation and characterization of Pt NPs

Three kinds of Pt NPs were obtained. M-Pt NPs and R-Pt NPs were synthesized as controls to prove the different function of I-Pt NPs. M-Pt NPs had mPEG as capping agents and exhibited PTT and ensuing DCs maturation. The capping agent for R-Pt NPs was the rhodamine B (RhB)-furan-Mal-functionalized PEG (R-PEG$_{2k}$), which had the additional function of antigen-capturing. Finally, BMS-1-furan-Mal-functionalized PEG (I-PEG$_{2k}$) endowed the I-Pt NPs with all the above properties, along with PD-1/PD-L1 blockade. I-PEG$_{2k}$ and R-PEG$_{2k}$ were obtained by esterifying BMS-1 (PD-L1 inhibitor) or RhB with furfuryl alcohol and

conjugating to Mal-functionalized carboxyl-PEG$_{2k}$ (Mal-PEG$_{2k}$-COOH) *via* a Diels–Alder reaction between furan and Mal groups (Fig. S1). The synthesis of furfuryl BMS-1 (or furfuryl RhB) was verified by ^{1}H-NMR and electrospray ionization mass spectrometry (ESI-MS) (Fig. S2-3) and that of R-PEG$_{2k}$ and I-PEG$_{2k}$ by ^{1}H-NMR (Fig. S4-5). All three kinds of Pt NPs in this work were synthesized by reducing K$_2$PtCl$_4$ with NaBH$_4$ in the presence of mPEG$_{2k}$-NH$_2$ [68,69]. M-Pt NPs, R-Pt NPs and I-Pt NPs were synthesized with mPEG$_{2k}$-COOH [70], R-PEG$_{2K}$-COOH and I-PEG$_{2k}$-COOH as the respective capping agents. The molar ratio of loading BMS-1 to Pt in the synthesized Pt NPs is 1:1. As shown in the TEM images in Fig. 1a, the Pt NPs showed a homogeneous size distribution. The broad characteristic X-ray diffraction (XRD) peaks at 39.46 (111), 45.88 (200) and 67.32 (220) corresponded to the face center-cubic (f.c.c.) structure of standard Pt NPs (JCPDS, card no. 4-802) [71–73] (Fig. 1b). UV–vis spectroscopy and high-resolution Pt$_{4f}$ XPS spectrum also confirmed the Pt NPs structure [74,75], which laid the basic foundation for the photothermal convertion. (Fig. 1c and Fig. S6a). The hydrodynamic size of M-Pt NPs, R-Pt NPs and I- Pt NPs were 5.615 nm, 4.849 nm and 4.849 nm respectively, and the ζ potential were −4.9 eV, −7.2 eV and −5.1 eV (pH 6.0) and −19.9 eV, −15.7 eV and −20.5 eV (pH 7.0) according to dynamic light scattering (DLS) measurements (Fig. 1d and e). Pt NPs of varying concentrations were irradiated with an 808 nm laser at 0.8 W/cm^2 for 10 min, and different laser power outputs were used to illuminate 0.22 mM Pt NPs (Fig. 1f and Fig. S6b) to obtain heating curves. As shown in Fig. S6c, all Pt NPs were photothermally stable even after five cycles of heating and cooling [76,77]. The photothermal conversion efficiency of Pt NPs was calculated as 14.76% as previously described (Fig. S6d, e) [78].

3.2. Pt NPs released BMS-1 and captured tumor antigens in response to NIR light

[4 + 2] cycloaddition between a diene and a dienophile shows thermal reversibility [79–81]. The retro-Diels-Alder reaction, or diene/dienophile generation from cyclohexane, can be stimulated by NIR irradiation [82–84]. This is the first study to show that the photothermal effect of Pt NPs can achieve retro-Diels-Alder reaction. When the temperature of I-Pt NPs (or R-Pt NPs) aqueous solution was raised to 50 °C upon NIR exposure, the reverse reaction between furan and Mal resulted in the controlled release of BMS-1 (or RhB), along with the deprotection of Mal. As shown in Fig. 1g, the fluorescence emission from RhB was efficiently quenched by the Pt NPs in the absence of any photothermal effect. However, NIR (808 nm, 0.8 W/cm^2) triggered release of RhB from the Pt NPs surface showed significant fluorescence emission [57] (Fig. S6g and Fig. 1h), and the intensity of fluorescence increased in a time-dependent manner (Fig. S6h). The fluorescence spectra of the released RhB were consistent with that of standard RhB (Fig. S6f). Likewise, the BMS-1 was released after 2 min of NIR exposure and the amount increased with prolonged irradiation (Fig. 1i and Fig. S6i). In addition, Mal was de-protected on the surface of Pt NPs and characterized by ^{1}H-NMR. The specific chemical shift of Mal re-appeared on ^{1}H-NMR after photothermal conversion (Fig. S7).

The exposed Mal groups at the end of PEG chains captured tumor antigens through the reaction with the protein sulfhydryl groups. As shown in Fig. 1j, the diameter of R-Pt NPs and I-Pt NPs (after illumination) incubated with ovalbumin (OVA) was significantly greater compared to control particles, indicating successful antigen-capturing. Consistent with this, the zeta potential of the I-Pt NPs (after illumination) incubated with OVA decreased from −4.5 mV to −16.6 mV and the R-Pt NPs decreased from −7.7 mV to −17.4 mV. While M-Pt NPs showed few changes in diameter and zeta potential (Fig. 1k). The different Pt NPs (1 mM) were incubated with 4T1 cells (24 h) and illuminated with NIR (808 nm, 0.8 W/cm^2). The uptake of Pt NPs was evaluated by ICP (Fig. S10b). The prepared Pt NPs were slightly toxic at dark, but cell survival was significantly reduced under light conditions (Fig. S10a). At the same time, the amounts of antigens captured by I-Pt-NPs increased
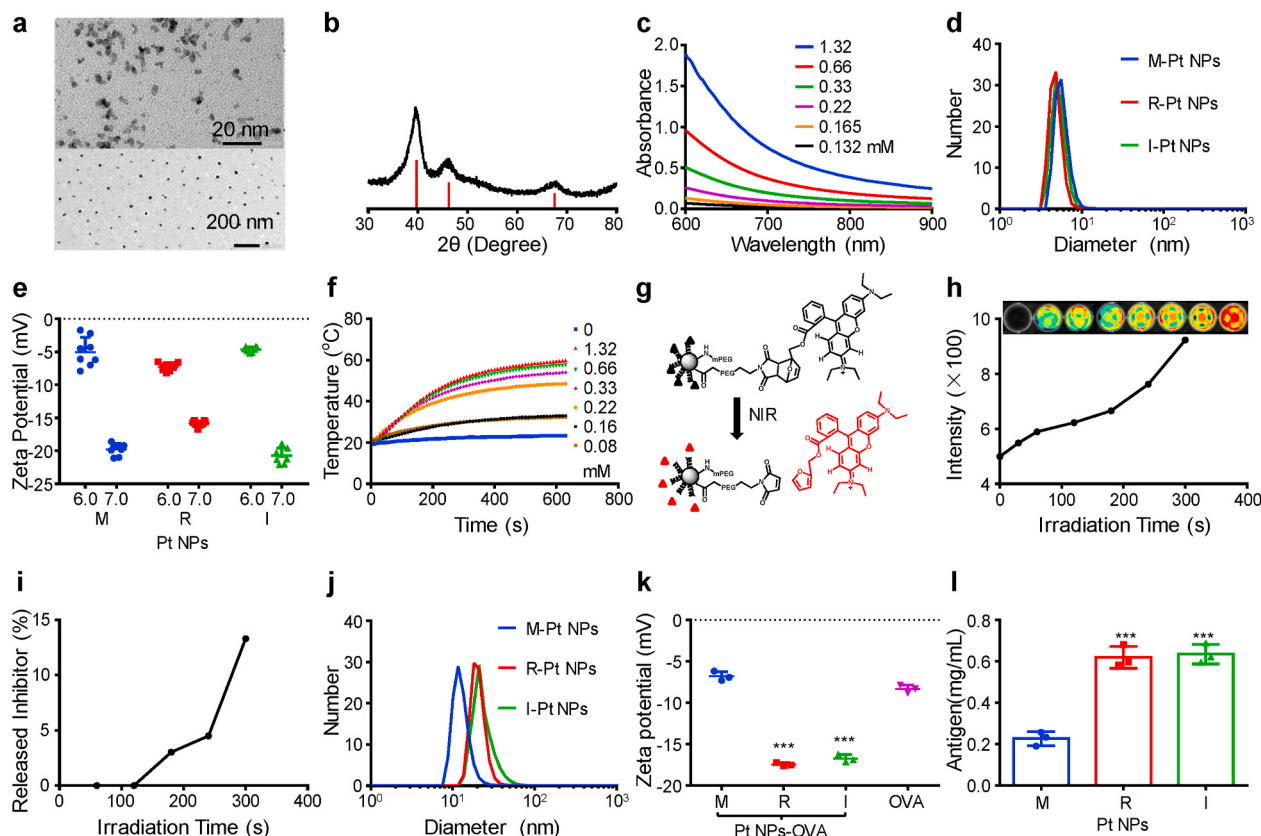
Fig. 1. Characterization of Pt NPs. (a) TEM images (Scale bars: upper: 20 nm; lower: 200 nm) and (b) XRD of Pt NPs. (c) Absorption spectra of Pt NPs at various concentrations. (d) Hydrodynamic diameters and (e) Zeta potential of Pt NPs, R-Pt NPs, I-Pt NPs at pH 6.0 and pH 7.0. (f) Temperature elevation of Pt NPs at various concentrations under 0.8 W/cm^2 irradiation (808 nm, 10 min). (g) NIR-stimulated release of RhB. (h) Fluorescence imaging and calculation of 1 mM R-Pt NPs upon irradiation (808 nm, 0.8 W/cm^2) as a function of time. (i) Time-dependent inhibitor release profiles of 1 mM I-Pt NPs in response to NIR (808 nm, 0.8 W/cm^2). (j) The diameter of Pt NPs (+) after incubation with OVA. (k) Zeta potential of Pt NPs after incubation with OVA. (l) Quantification of proteins captured by Pt-NPs after incubating with 4T1 cells under 0.8 W/cm^2 irradiation (808 nm, 5 min). Data are presented as the mean $\pm$ SEM. The (+) refers to laser irradiation 808 nm, 0.8 W/cm^2, 5 min $*p < 0.05$, $**p < 0.01$ and $***p < 0.001$ from control by *t*-test.

gradually as irradiation time goes by (Fig. S10c). The R-Pt NPs and I-Pt NPs captured 0.61 mg/mL and 0.62 mg/mL tumor proteins respectively compared to only 0.2 mg/mL by the M-Pt NPs (Fig. 1l).

3.3. Pt NPs induced DC maturation and antigen-capturing function

To evaluate the adjuvant function of Pt NPs, DC2.4 cells were incubated with different concentrations of Pt NPs or 0.1 μg/mL lipopolysaccharides (LPS) for 24 h and labeled with CD80-FITC. As shown in Fig. 2a, the proportion of CD80$^+$ mature DCs increased significantly in the presence of the Pt-NPs in a concentration-dependent manner, indicating that Pt NPs acted as an adjuvant and induced DC maturation. Likewise, mice injected with 1.25 and 2.5 mg/kg Pt NPs had respectively 5 and 6-fold higher numbers of mature DCs in the nearest lymph nodes compared to the controls (Fig. 2b and Fig. S8a).

Given the selective accumulation of Pt NPs in the lymph nodes (Fig. 2l, m), it raises the possibility of Pt NPs transporting the tumor antigens released during PTT into the lymph nodes *via* the DC cells, and eliciting an immune response after antigen presentation. In fact, ultra-small nanoparticles are known to accumulate in lymphatic capillaries and nodes through lymphatic drainage [85,86]. In addition, mobilizing the resident DCs of lymph nodes can achieve sustained delivery of antigens and immunomodulatory substances to professional APCs in the lymphoid environment [87]. FITC-OVA were synthesized as previously described to represent antigens released from ablated tumor cells. It was found that the antigen captured by R-Pt NPs were more likely to be engrafted by bone marrow-derived DCs (BMDCs) (Fig. 2c and Fig. S8b),

and accumulated in the nearest lymph nodes (Fig. 2n).

To further validate the effect of Pt NPs-induced PTT on DC maturation, primary murine BMDCs were incubated the debris of Pt NPs-ablated 4T1 cells in a transwell system (Fig. 2d). Following incubation with M-Pt NPs and 4T1 cells in the dark, the proportion of mature (CD80$^+$CD86$^+$) DC cells increased slightly from 36.5% (control) to 41.4%, indicating the inherent adjuvant function of Pt NPs. Upon NIR irradiation, however, R-Pt NPs and M-Pt NPs respectively increased the proportion of mature DCs to 61.8% and 45% in the presence of 4T1 cells (Fig. 2e and Fig. S9a). These findings indicated that the Pt NPs acted as adjuvants that promote DC maturation, and antigen-capturing of R-Pt NPs exceeded M-Pt NPs due to increased recognition and endocytosis of the captured antigens by DC cells. Consistent with this, BMDCs stimulated with R-Pt NPs (+) treated 4T1 cells secrete higher amounts of IL-12p70 and IL-1β compared to unstimulated cells (Fig. S9b, c), indicating that antigens released from photothermally ablated tumor cells strongly promote DC maturation and activation.

For *in vivo* evaluation, the 4T1 tumor-bearing mice were intra-tumorally injected with Pt NPs (dose = 1.25 mg Pt/kg) with (+) or without NIR laser irradiation (808 nm, 0.8 W/cm^2, 5 min). The mice were sacrificed 12 h post-treatment and the maturation status of DCs in tumor draining lymph nodes (TDLN) was analyzed. The proportion of CD11c$^+$ DC cells increased from 2.58% to 9.91% in the non-irradiated mice treated with M-Pt NPs, and to 13% in the irradiated counterparts. The combination of R-Pt NPs and NIR radiation significantly increased the proportion of DCs to 16.86% (Fig. 2f and Fig. S9d). In addition, the proportion of mature (CD80$^+$CD86$^+$) DC cells in the TDLN
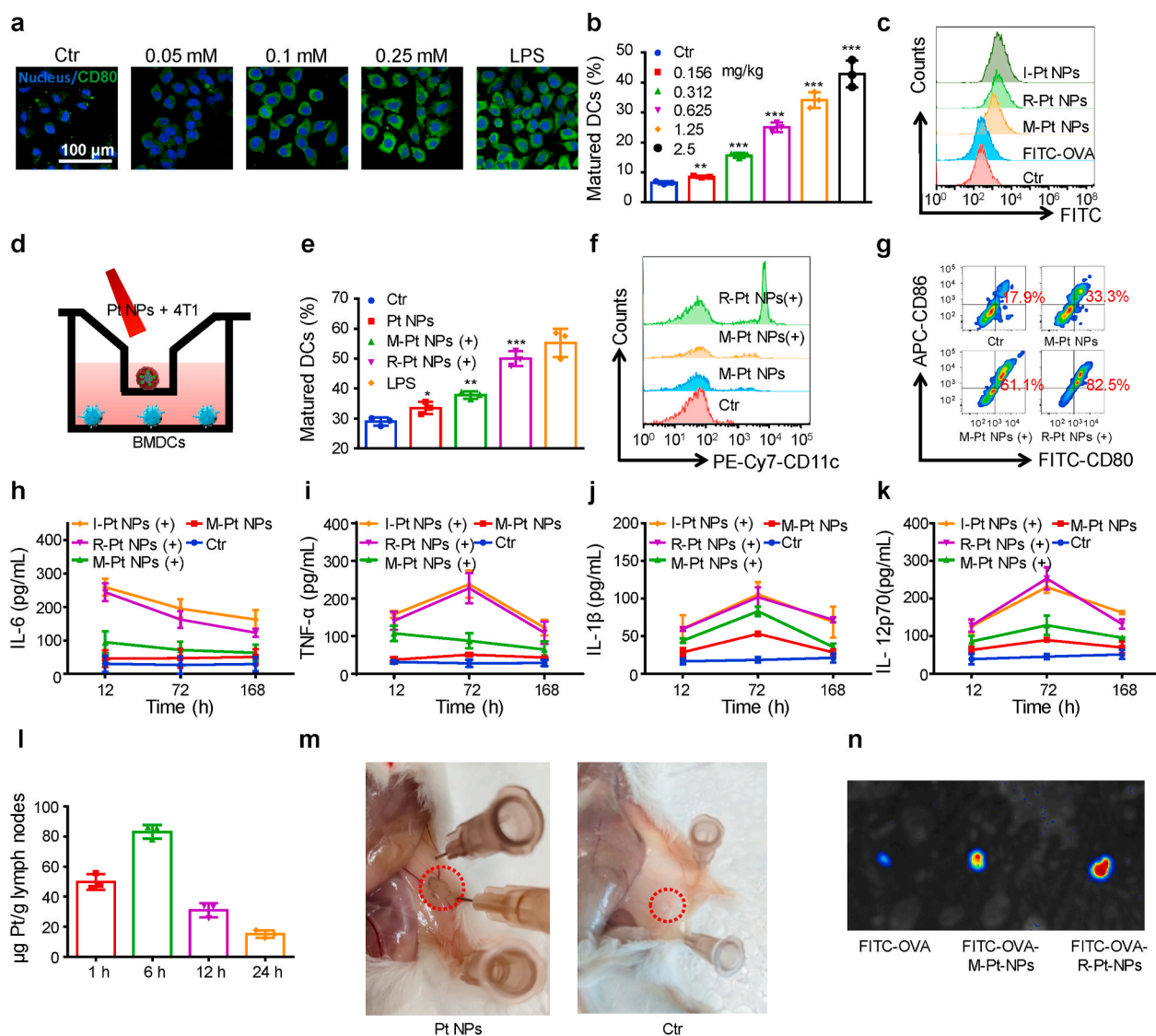
Fig. 2. Pt NPs-induced PTT promotes DC maturation and stimulates the expression of pro-inflammatory cytokines. (a) Representative CLSM image of CD80$^+$ DC2.4 cells incubated with Pt NPs or LPS. (b) Percentage of CD11c$^+$CD80$^+$CD86$^+$ DCs in the nearest lymph nodes after subcutaneous administration of M-Pt NPs. (c) Flow cytometry histogram showing FITC-OVA internalization by BMDCs. (d) Schematic representation of the transwell system. (e) Percentage of mature BMDCs after R-Pt NPs-based PTT (or Pt NPs-based PTT) in the transwell system. (f) Percentage of CD11c$^+$ DCs in the TDLN. (g) Representative FACS plots showing percentage of CD80$^+$CD86$^+$CD11c$^+$ cells in TDLN. (h-k) Cytokine levels in the sera of mice at 12 h, 72 h and 168 h post M-Pt NPs, M-Pt NPs (+) R-Pt NPs (+) and I-Pt NPs (+). (l) The accumulation of Pt in the nearest lymph nodes analyzed by ICP. (m) Image of the nearest lymph nodes after subcutaneous administration of Pt NPs (left) and without administration of Pt NPs (right). (n) The accumulation of FITC-OVA-Pt NPs in the nearest lymph nodes. Data are presented as the mean ± SEM. The (+) refers to laser irradiation 808 nm, 0.8 W/cm^2, 5 min *$p < 0.05$, **$p < 0.01$ and ***$p < 0.001$ from control by *t*-test.

of mice treated with M-Pt NPs, M-Pt NPs (+) and R-Pt NPs (+) were 33.3%, 61.1% and 82.5% respectively compared to only 17.9% in the untreated control (Fig. 2g and Fig. S9e).

The serum levels of IL-12, IL-1β, IL-6 and tumor necrosis factor α (TNF-α) on day 3 were significantly higher in tumor-bearing mice treated with Pt NPs-based PTT (dose = 1.25 mg Pt/kg), indicating an acute inflammatory response (Fig. 2h–k). IL-12 regulates the activity of natural killer (NK) cells, whereas TNF-α is a critical mediator of anti-tumor cellular immunity [88,89]. Taken together, the adjuvant function of R-Pt NPs and I-Pt NPs markedly improved the anti-tumor immune response *via* increased DC maturation and antigen-capturing.

3.4. Abscopal effect of Pt NPs-based PTT

PD-1/PD-L1 interaction leads to T cell exhaustion and consequently inhibits anti-tumor immune responses. BMS-1 block the PD-1/PD-L1 checkpoint by inducing dimerization of PD-L1, and have several advantages over antibody-based immunotherapies such as lower cost, extended half-life and low immunogenicity [90,91]. PD-L1 is frequently overexpressed on the surface of cancer cells, and soluble PD-L1 (sPD-L1) is elevated in the plasma of some cancer patients [92]. The combination of BMS-1 and antigen-capturing PTT can therefore synergize T cell activation and effective antigen presentation.

To assess the immunotherapeutic effects of Pt NP-based PTT, a bilateral tumor model were established. The primary tumors were injected with saline or the different Pt NPs and irradiated with NIR laser (808 nm, 0.8 W/cm^2, 5 min), whereas the secondary tumor was untreated (Fig. 3a). IR thermal imaging showed that the Pt NPs increased the temperature at the tumor site by 14.4 °C upon irradiation (Fig. 3b). The M-Pt NPs and R-Pt NPs had only a slight inhibitory effect on the tumors in the non-irradiated mice, whereas the I-Pt NPs significantly inhibited tumor growth even in the absence of NIR irradiation, which
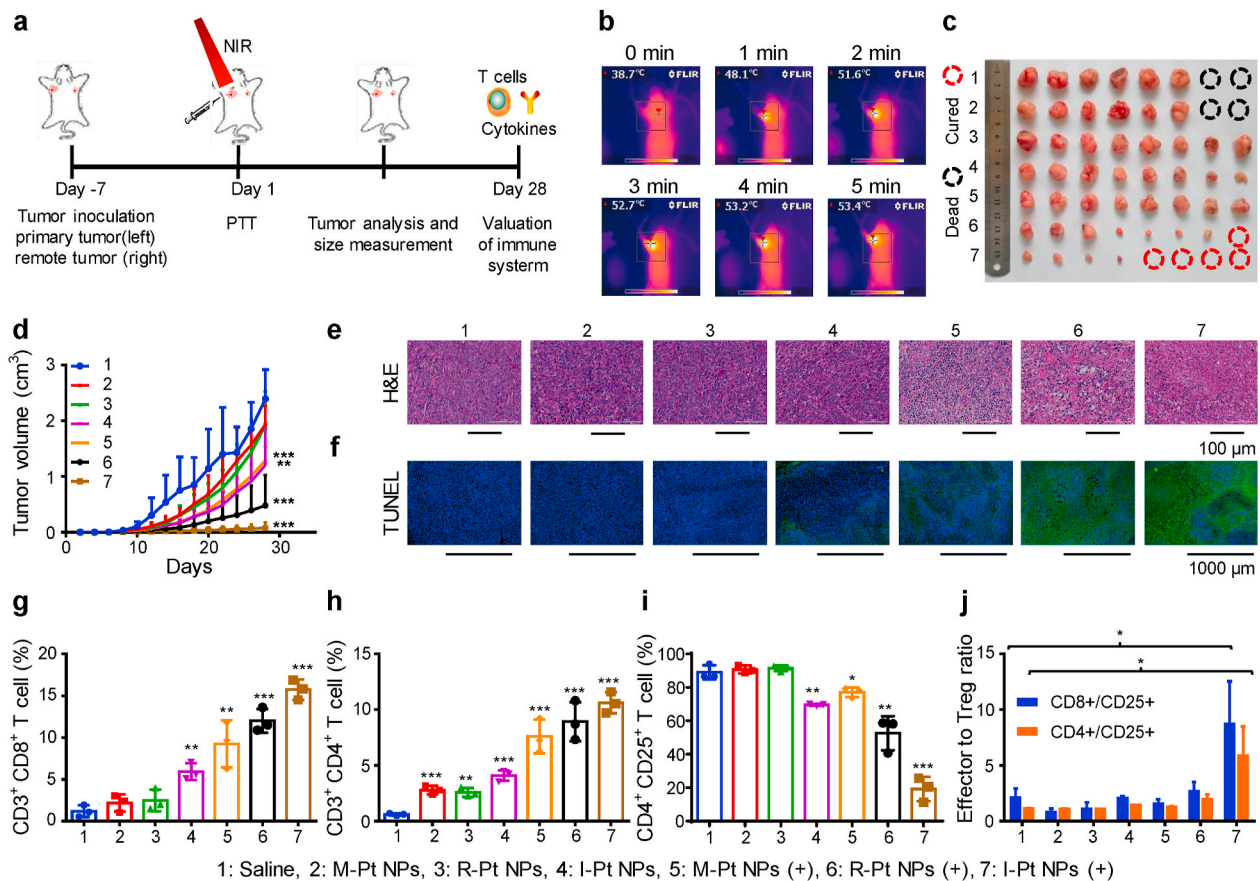
Fig. 3. Remote memory model of Pt NPs-induced PTT. (a) Schematic illustration of Pt NPs-induced PTT on a remote memory model. (b) Representative IR thermal images of tumor-bearing mice exposed to the NIR laser (808 nm, 0.8 W/cm², 5 min) after injection with Pt NPs. (c) Representative images of the excised second tumors on day 28 following different therapies. (d) Growth curves of the second tumor in the differentially treated mice (n = 8 per group). (e) Representative images of H&E stained sections of distant tumors in the indicated groups (scale bar = 100 μm). (f) Representative images of TUNEL stained distant tumor sections in the indicated groups (scale bar = 1000 μm). (g–j) Quantification of T cells in the secondary tumors of indicated groups: (g, h) Proportion of tumor-infiltrating CD8⁺ T cells and CD4⁺ T cells, (i) proportion of tumor-infiltrating CD4⁺ CD25⁺ T cells, and (j) ratio of effector to regulatory T cells in the secondary tumors. Data are presented as the mean ± SEM. The (+) refers to laser irradiation 808 nm, 0.8 W/cm², 5 min *$p < 0.05$, **$p < 0.01$ and ***$p < 0.001$ from control by *t*-test.

can be attributed to the inherent chemical toxicity of the Pt NPs. Furthermore, the greater inhibitory effect of the I-Pt NPs is likely due to PD-1/PD-L1 blockade. In the irradiated mice treated with M-Pt NPs, the average tumor volume increased to 1294 mm³ on day 28, whereas R-Pt NPs (+) and I-Pt NPs (+) restricted the tumor growth to 481 mm³ and 77 mm³ respectively (Fig. 3c, d and Fig. S11a). There was no significant weight loss or death in all groups, indicating the lack of any significant systematic toxicity of the drugs (Fig. S11c). Furthermore, biochemical indices of hepatic and renal function such as alanine aminotransferase (ALT), aspartate aminotransferase (AST), uric acid (UA), urea (UREA) and creatinine (CREA) were not markedly affected, indicating that there was no significant liver or kidney damage as well (Fig. S11d-h). Routine H&E staining and TUNEL assay showed that I-Pt NPs (+) significantly decreased the number of cancer cells and enhanced the apoptosis rates in the tumor tissue (Fig. 3e and f).

To determine the mechanism underlying secondary tumor inhibition, infiltration of T cells in the secondary tumors were evaluated on day 28 post-treatment. In the non-irradiated mice, the tumors treated with I-Pt NPs had more infiltrating CD8⁺ and CD4⁺ T cells compared to those treated with M-Pt NPs or R-Pt NPs. This strongly indicated that PD-1/PD-L1 checkpoint blockade enhanced T cell penetration. The activated intra-tumoral CD8⁺ T cells release cytotoxins, perforin, granzymes and granulysin that eventually trigger apoptosis in the residual cancer cells. We found that the percentage of CD8⁺ T cells in the secondary tumors was 2-fold higher in mice treated with I-Pt NPs (+) compared to M-Pt NPs (+), and that of the R-Pt NPs (+) group was 1.5-fold higher

relative to the M-Pt NPs (+) group (Fig. 3g and Fig. S12). Concomitantly, the regulatory T cells comprised 79.3% and 40.8% of the intra-tumoral CD4⁺CD25⁺ T cells in mice treated respectively with M-Pt NPs (+) and R-Pt NPs (+), which can hamper effective anti-tumor immune response. Furthermore, the CD8⁺/CD25⁺ T cell ratio was 4-fold higher and the CD4⁺/CD25⁺ T cell ratio was 5-fold higher in the I-Pt NPs (+) group compared to the control group (Fig. 3h, i, j and Fig. S13, 14). The stronger abscopal effect of R-Pt NPs (+) relative to M-Pt NPs (+) can be attributed to antigen-capturing by the former. Consistent with the effect of PD-1/PD-L1 blockade, the number of Tregs (CD3⁺CD4⁺CD25⁺) also decreased significantly in the I-Pt NPs (+) group compared to the R-Pt NPs (+) group. The serum levels of IL-12, IL-1β, IL-6 and TNF-α were significantly higher in all treated mice compared to the untreated control on day 28 (Fig. S15a-d), indicating that Pt NPs-induced PTT elicited a substantial level of immunological response. Thus, Pt NPs can photothermally enhance tumor-specific immune responses and inhibit tumor growth at distant sites.

3.5. Pt NPs-induced PTT prevented tumor recurrence by stimulating long term immune memory effects

To determine whether Pt NPs-induced PTT can prevent tumor recurrence by eliciting long-term immune memory, a recurrence and remote memory mouse model of 4T1 were established (Fig. 4a). Mice subjected to I-Pt NPs-based PTT had minimum recurrence rate compared to the R-Pt NPs and M-Pt NPs groups (Fig. 4b). In addition, I-Pt NPs-
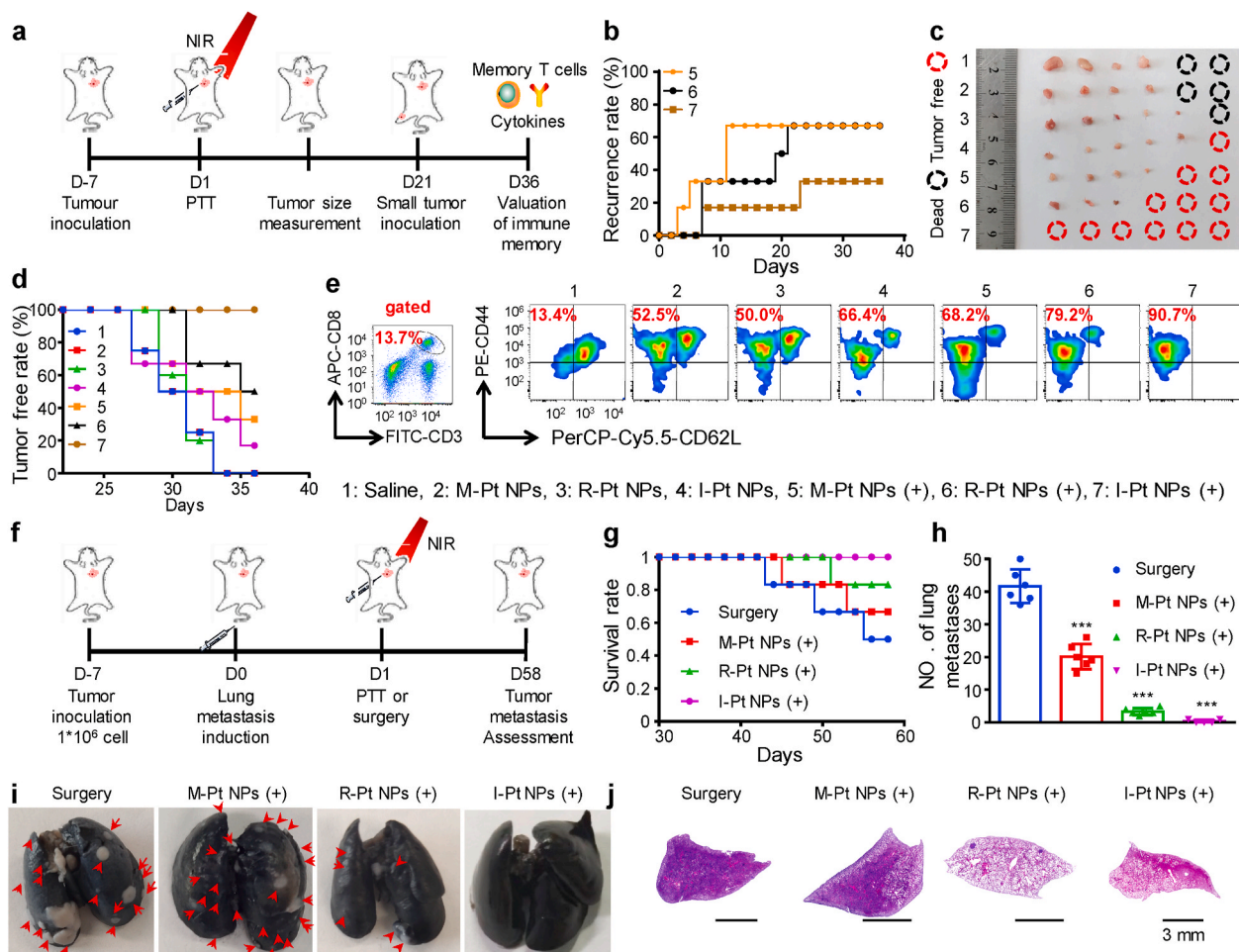
Fig. 4. Pt NPs-induced PTT prevented tumor recurrence and lung metastasis by triggering long-term immune memory. (a) Schematic illustration of the recurrence model. (b) Recurrence rate after PTT on day 1. (c) Representative images of regenerated tumors. (d) Tumor free rate after day 21 post-inoculation. (e) FACS plots showing percentage of T_{EM} cells in the spleen (gated on $CD3^+CD8^+T$ cells). (f) Schematic illustration of lung metastasis model. (g) Survival rate of mice in the indicated groups. (h) Number of metastatic nodules in the lungs. (i-j) Representative images of (i) the India ink-stained whole lungs (Lung metastatic nodules were marked by the red arrows) and (j) H&E-stained tissue sections (scale bar = 3 mm). Data are presented as the mean ± SEM. The (+) refers to laser irradiation 808 nm, 0.8 W/cm^2, 5 min ***$p < 0.001$ from control by *t*-test. (For interpretation of the references to colour in this figure legend, the reader is referred to the Web version of this article.)

based PTT significantly decreased the tumor volume and tumor weight (Fig. S16a-c). M-Pt NPs and R-Pt NPs slightly inhibited tumor growth compared to the untreated control even in the absence of NIR irradiation, implying potential chemotoxicity of Pt NPs. The I-Pt NPs showed greater tumor inhibition in comparison to the other Pt-NPs due to PD-1/PD-L1 immune checkpoint blockade. Since the tumor cells remaining after PTT are the main cause of tumor relapse, the immune response elicited by PTT, antigen-capturing and PD-L1 blockade can eliminate the residual tumor cells and prevent recurrence. R-Pt NPs (+) resulted in greater tumor inhibition compared to M-Pt NPs (+) since antigen-capturing by R-Pt NPs (+) facilitated antigen presentation after PTT. Furthermore, the mice treated with I-Pt NPs (+) showed least relapse given that the increased infiltration of effector T cells can clear the residual tumor cells after PTT. There was no significant weight loss in any of the treatment groups, indicating low systemic toxicity (Fig. S16d). Several mice in the Saline, M-Pt NPs and R-Pt NPs were euthanized due to large tumor volume, and the survival rates were 66.7% in the saline and M-Pt NPs groups, and 88.3% in the R-Pt NPs group over 35 days. In contrast, no deaths were recorded in the NIR-irradiated groups (Fig. 4e). On day 21, 4×10^5 tumor cells were injected subcutaneously into the left leg, and tumor growth was monitored for 2 weeks (Fig. 4d). The PTT induced by I-Pt NPs and R-Pt NPs decreased the tumor formation rate after the secondary inoculation to 67% and 50% respectively (Fig. 4c),

which can be attributed to the increase in effector memory T cells that induce a strong immune memory protection by secreting TNF-α and IFN-γ [93,94]. Indeed, mice treated with the different Pt NPs and NIR radiation exhibited significantly higher frequencies of effector memory T cells ($CD3^+CD8^+CD62L^-CD44^+$) compared to the untreated controls (Fig. 4e and Fig. S16f). Taken together, Pt NPs-based PTT can also induce tumor-specific immune memory responses and thereby inhibit tumor regrowth and relapse.

3.6. Pt NPs-induced PTT inhibited lung metastasis

To assess the anti-metastatic effect of Pt NPs-induced PTT, a model of lung metastasis were established by intravenously injecting mice with 4T1 cells (1×10^5 cells per mouse) (Fig. 4f). All mice treated with I-Pt NPs (+) survived for at least 58 days, whereas the survival rate in the R-Pt NPs (+) group over the duration was 83.3%. In contrast, only 50% mice survived after surgery and 66.7% after M-Pt NPs (+) (Fig. 4g). I-Pt NPs-induced PTT markedly reduced the number of lung metastatic nodules, as indicated by the India ink-stained whole lungs and H&E stained lung slices [95] (Fig. 4h–j). Taken together, Pt NPs-induced photothermal ablation of the primary tumor and the release of BMS-1 can elicit a strong anti-tumor immunological response to inhibit lung metastasis.

4. Conclusion

We fabricated photothermal-sensitive PEG-capped Pt NPs that ablated tumor cells through PTT and amplified the anti-tumor immune response synergistically by acting as an adjuvant. NIR radiation further facilitated the hyperthermia-triggered exposure of Mal on Pt NPs and release of BMS-1. Exposed Mal captured the ablated tumor antigens and transported them to DCs, which promoted the antigen presentation process. In addition, BMS-1 relieved T cell exhaustion and enhanced infiltration in the tumor microenvironment. The combination of PTT with immunotherapy inhibited the growth of remained cancer cells in a subcutaneous memory tumor model, the growth of the secondary tumor in a remote tumor model and the growth of metastasis tumor cells in a lung metastasis model. The photo sensitive I-Pt NPs are promising nanomaterials against cancer relapse and metastasis.

Author contributions

J. Y. performed experiments and analyses. S. L., Y. W., X. H., and Q. Z. performed the flow cytometry and ELISA tests in animal tissue. D. Z. and Z. X. contributed to data curation and supervision. Y. Q., X. L. and Y. H. contributed to project administration. The manuscript was written through contributions of all authors. All authors have given approval to the final version of the manuscript.

CRediT authorship contribution statement

Jie Yu: performed experiments and analyses. **Yupeng Wang:** performed the flow cytometry, ELISA tests in animal tissue. **Xidong He:** performed the flow cytometry, ELISA tests in animal tissue. **Qingfei Zhang:** performed the flow cytometry, ELISA tests in animal tissue. **Yanxin Qi:** contributed to Project administration. **Xiaoyuan Li:** contributed to Project administration. **Yubin Huang:** contributed to Project administration, The manuscript was written through contributions of all authors. All authors have given approval to the final version of the manuscript.

Declaration of competing interest

The work described here is original and has not been published previously, and not under consideration for publication elsewhere. All the authors listed have approved the submission of this manuscript. The authors declare no competing interests.

Appendix A. Supplementary data

Supplementary data to this article can be found online at https://doi.org/10.1016/j.bioactmat.2021.05.030.

References

[1] Q. Zhang, X. Guo, Y. Cheng, L. Chudal, N.K. Pandey, J. Zhang, L. Ma, Q. Xi, G. Yang, Y. Chen, X. Ran, C. Wang, J. Zhao, Y. Li, L. Liu, Z. Yao, W. Chen, Y. Ran, R. Zhang, Use of copper-cysteamine nanoparticles to simultaneously enable radiotherapy, oxidative therapy and immunotherapy for melanoma treatment, Signal Transduct Target Ther 5 (1) (2020) 58, https://doi.org/10.1038/s41392-020-0156-4.

[2] M. Yao, L. Ma, L. Li, J. Zhang, R. Lim, W. Chen, Y. Zhang, A new modality for cancer treatment–nanoparticle mediated microwave induced photodynamic therapy, J. Biomed. Nanotechnol. 12 (10) (2016) 1835–1851, https://doi.org/10.1166/jbn.2016.2322.

[3] X. Chu, K. Li, H. Guo, H. Zheng, S. Shuda, X. Wang, J. Zhang, W. Chen, Y. Zhang, Exploration of graphitic-C3N4 quantum dots for microwave-induced photodynamic therapy, ACS Biomater. Sci. Eng. 3 (8) (2017) 1836–1844, https://doi.org/10.1021/acsbiomaterials.7b00110.

[4] X. Chu, L. Mao, O. Johnson, K. Li, J. Phan, Q. Yin, L. Li, J. Zhang, W. Chen, Y. Zhang, Exploration of TiO2 nanoparticle mediated microdynamic therapy on cancer treatment, Nanomed. Nanotechnol. Biol. Med. 18 (2019) 272–281, https://doi.org/10.1016/j.nano.2019.02.016.

[5] K.F. Chu, D.E. Dupuy, Thermal ablation of tumours: biological mechanisms and advances in therapy, Nat. Rev. Canc. 14 (3) (2014) 199–208, https://doi.org/10.1038/nrc3672.

[6] Y. Zhou, X. Ren, Z. Hou, N. Wang, Y. Jiang, Y. Luan, Engineering a photosensitizer nanoplatform for amplified photodynamic immunotherapy via tumor microenvironment modulation, Nanoscale Horiz. 6 (2) (2021) 120–131, https://doi.org/10.1039/d0nh00480d.

[7] J.P. Almeida, R.A. Drezek, A.E. Foster, Controlling melanoma at local and systemic levels: is a combination of ablative therapy and immunotherapy the way forward? Immunotherapy 6 (2) (2014) 109–111, https://doi.org/10.2217/imt.13.158.

[8] R. Waitz, S.B. Solomon, E.N. Petre, A.E. Trumble, M. Fasso, L. Norton, J.P. Allison, Potent induction of tumor immunity by combining tumor cryoablation with anti-CTLA-4 therapy, Cancer Res. 72 (2) (2012) 430–439, https://doi.org/10.1158/0008-5472.CAN-11-1782.

[9] M.H. den Brok, R.P. Sutmuller, R. van der Voort, E.J. Bennink, C.G. Figdor, T.J. Ruers, G.J. Adema, In situ tumor ablation creates an antigen source for the generation of antitumor immunity, Cancer Res. 64 (11) (2004) 4024–4029, https://doi.org/10.1158/0008-5472.CAN-03-3949.

[10] R. Ge, C. Liu, X. Zhang, W. Wang, B. Li, J. Liu, Y. Liu, H. Sun, D. Zhang, Y. Hou, H. Zhang, B. Yang, Photothermal-activatable Fe3O4 superparticle nanodrug carriers with PD-L1 immune checkpoint blockade for anti-metastatic cancer immunotherapy, ACS Appl. Mater. Interfaces 10 (24) (2018) 20342–20355, https://doi.org/10.1021/acsami.8b05876.

[11] D. Liu, B. Chen, Y. Mo, Z. Wang, T. Qi, Q. Zhang, Y. Wang, Redox-activated porphyrin-based liposome remote-loaded with indoleamine 2,3-dioxygenase (IDO) inhibitor for synergistic photoimmunotherapy through induction of immunogenic cell death and blockage of IDO pathway, Nano Lett. 19 (10) (2019) 6964–6976, https://doi.org/10.1021/acs.nanolett.9b02306.

[12] Q. Chen, J. Chen, Z. Yang, J. Xu, L. Xu, C. Liang, X. Han, Z. Liu, Nanoparticle-enhanced radiotherapy to trigger robust cancer immunotherapy, Adv. Mater. 31 (10) (2019), e1802228, https://doi.org/10.1002/Adma.201802228.

[13] A.P. Castano, P. Mroz, M.X. Wu, M.R. Hamblin, Photodynamic therapy plus low-dose cyclophosphamide generates antitumor immunity in a mouse model, Proc. Natl. Acad. Sci. U.S.A. 105 (14) (2008) 5495–5500, https://doi.org/10.1073/pnas.0709256105.

[14] W.R. Chen, A.K. Singhal, H. Liu, R.E. Nordquist, Antitumor immunity induced by laser immunotherapy and its adoptive transfer, Cancer Res. 61 (2) (2001) 459–461. http://cancerres.aacrjournals.org/cgi/content/abstract/61/2/459.

[15] Y. Zhang, T. Song, T. Feng, Y. Wan, N.T. Blum, C. Liu, C. Zheng, Z. Zhao, T. Jiang, J. Wang, Q. Li, J. Lin, L. Tang, P. Huang, Plasmonic modulation of gold nanotheranostics for targeted NIR-II photothermal-augmented immunotherapy, Nano Today 35 (2020), 100987, https://doi.org/10.1016/j.nantod.2020.100987.

[16] D.M. Smith, J.K. Simon, J.R. Baker Jr., Applications of nanotechnology for immunology, Nat. Rev. Immunol. 13 (8) (2013) 592–605, https://doi.org/10.1038/nri3488.

[17] S.R. Gameiro, J.P. Higgins, M.R. Dreher, D.L. Woods, G. Reddy, B.J. Wood, C. Guha, J.W. Hodge, Combination therapy with local radiofrequency ablation and systemic vaccine enhances antitumor immunity and mediates local and distal tumor regression, PloS One 8 (7) (2013), e70417, https://doi.org/10.1371/journal.pone.0070417.

[18] J. Zhang, N. Wang, Q. Li, Y. Zhou, Y. Luan, A two-pronged photodynamic nanodrug to prevent metastasis of basal-like breast cancer, Chem. Commun. 57 (18) (2021) 2305–2308, https://doi.org/10.1039/D0CC08162K.

[19] D. Chen, C. Zhao, J. Ye, Q. Li, X. Liu, M. Su, H. Jiang, C. Amatore, M. Selke, X. Wang, In situ biosynthesis of fluorescent platinum nanoclusters: toward self-bioimaging-guided cancer theranostics, ACS Appl. Mater. Interfaces 7 (32) (2015) 18163–18169, https://doi.org/10.1021/acsami.5b05805.

[20] M.S. Shoshan, T. Vonderach, B. Hattendorf, H. Wennemers, Peptide-coated platinum nanoparticles with selective toxicity against liver cancer cells, Angew. Chem. Int. Ed. 58 (15) (2019) 4901–4905, https://doi.org/10.1002/anie.201813149.

[21] H. Xia, F. Li, X. Hu, W. Park, S. Wang, Y. Jang, Y. Du, S. Baik, S. Cho, T. Kang, D.-H. Kim, D. Ling, K.M. Hui, T. Hyeon, pH-sensitive Pt nanocluster Assembly overcomes cisplatin resistance and heterogeneous stemness of hepatocellular carcinoma, ACS Cent. Sci. 2 (11) (2016) 802–811, https://doi.org/10.1021/acscentsci.6b00197.

[22] J. Gao, G. Liang, B. Zhang, Y. Kuang, X. Zhang, B. Xu, FePt@CoS2Yolk−Shell nanocrystals as a potent agent to kill HeLa cells, J. Am. Chem. Soc. 129 (5) (2007) 1428–1433, https://doi.org/10.1021/ja067785e.

[23] E.J. Cho, B. Sun, K.O. Doh, E.M. Wilson, S. Torregrosa-Allen, B.D. Elzey, Y. Yeo, Intraperitoneal delivery of platinum with in-situ crosslinkable hyaluronic acid gel for local therapy of ovarian cancer, Biomaterials 37 (2015) 312–319, https://doi.org/10.1016/j.biomaterials.2014.10.039.

[24] H.J. Cheng, T.H. Wu, C.T. Chien, H.W. Tu, T.S. Cha, S.Y. Lin, Corrosion-activated chemotherapeutic function of nanoparticulate platinum as a cisplatin resistance-

overcoming prodrug with limited autophagy induction, Small 12 (44) (2016) 6124–6133, https://doi.org/10.1016/j.biomaterials.2014.10.039.

[25] Y. Tang, T. Yang, Q. Wang, X. Lv, X. Song, H. Ke, Z. Guo, X. Huang, J. Hu, Z. Li, P. Yang, X. Yang, H. Chen, Albumin-coordinated assembly of clearable platinum nanodots for photo-induced cancer theranostics, Biomaterials 154 (2017) 248–260, https://doi.org/10.1016/j.biomaterials.2017.10.030.

[26] H. Yang, L.Q. He, Y.W. Hu, X. Lu, G.R. Li, B. Liu, B. Ren, Y. Tong, P.P. Fang, Quantitative detection of photothermal and photoelectrocatalytic effects induced by SPR from Au@Pt nanoparticles, Angew. Chem. Int. Ed. 54 (39) (2015) 11462–11466, https://doi.org/10.1002/anie.201505985.

[27] Z. Zhou, Y. Wang, Y. Yan, Q. Zhang, Y. Cheng, Dendrimer-templated ultrasmall and multifunctional photothermal agents for efficient tumor ablation, ACS Nano 10 (4) (2016) 4863–4872, https://doi.org/10.1021/acsnano.6b02058.

[28] W. He, Y. Liu, J. Yuan, J.-J. Yin, X. Wu, X. Hu, K. Zhang, J. Liu, C. Chen, Y. Ji, Y. Guo, Au@Pt nanostructures as oxidase and peroxidase mimetics for use in immunoassays, Biomaterials 32 (4) (2011) 1139–1147, https://doi.org/10.1016/j.biomaterials.2010.09.040.

[29] C. Wang, X. Cai, J. Zhang, X. Wang, Y. Wang, H. Ge, W. Yan, Q. Huang, J. Xiao, Q. Zhang, Y. Cheng, Trifolium-like platinum nanoparticle-mediated photothermal therapy inhibits tumor growth and osteolysis in a bone metastasis model, Small 11 (17) (2015) 2080–2086, https://doi.org/10.1002/smll.201403315.

[30] M. Manikandan, N. Hasan, H.F. Wu, Platinum nanoparticles for the photothermal treatment of Neuro 2A cancer cells, Biomaterials 34 (23) (2013) 5833–5842, https://doi.org/10.1016/j.biomaterials.2013.03.077.

[31] Y. Ma, Y. Zhang, X. Li, Y. Zhao, M. Li, W. Jiang, X. Tang, J. Dou, L. Lu, F. Wang, Y. Wang, Near-infrared II phototherapy induces deep tissue immunogenic cell death and potentiates cancer immunotherapy, ACS Nano 13 (10) (2019) 11967–11980, https://doi.org/10.1021/acsnano.9b06040.

[32] B. Ding, P. Zheng, F. Jiang, Y. Zhao, M. Wang, M. Chang, P.a. Ma, J. Lin, MnOx nanospikes as nanoadjuvants and immunogenic cell death drugs with enhanced antitumor immunity and antimetastatic effect, Angew. Chem. Int. Ed. 59 (38) (2020) 16381–16384, https://doi.org/10.1002/anie.202005111.

[33] C. Wang, L. Xu, C. Liang, J. Xiang, R. Peng, Z. Liu, Immunological responses triggered by photothermal therapy with carbon nanotubes in combination with anti-CTLA-4 therapy to inhibit cancer metastasis, Adv. Mater. 26 (48) (2014) 8154–8162, https://doi.org/10.1002/adma.201402996.

[34] K. Niikura, T. Matsunaga, T. Suzuki, S. Kobayashi, H. Yamaguchi, Y. Orba, A. Kawaguchi, H. Hasegawa, K. Kajino, T. Ninomiya, K. Ijiro, H. Sawa, Gold nanoparticles as a vaccine platform: influence of size and shape on immunological responses in vitro and in vivo, ACS Nano 7 (5) (2013) 3926–3938, https://doi.org/10.1021/nn3057005.

[35] W. Wang, X. Zhou, Y. Bian, S. Wang, Q. Chai, Z. Guo, Z. Wang, P. Zhu, H. Peng, X. Yan, W. Li, Y.X. Fu, M. Zhu, Dual-targeting nanoparticle vaccine elicits a therapeutic antibody response against chronic hepatitis B, Nat. Nanotechnol. 15 (5) (2020) 406–416, https://doi.org/10.1038/s41565-020-0648-y.

[36] D.J. Irvine, M.C. Hanson, K. Rakhra, T. Tokatlian, Synthetic nanoparticles for vaccines and immunotherapy, Chem. Rev. 115 (19) (2015) 11109–11146, https://doi.org/10.1021/acs.chemrev.5b00109.

[37] K. Shao, S. Singha, X. Clemente-Casares, S. Tsai, Y. Yang, P. Santamaria, Nanoparticle-based immunotherapy for cancer, ACS Nano 9 (1) (2015) 16–30, https://doi.org/10.1021/nn5062029.

[38] R.H. Fang, A.V. Kroll, L. Zhang, Nanoparticle-based manipulation of antigen-presenting cells for cancer immunotherapy, Small 11 (41) (2015) 5483–5496, https://doi.org/10.1002/smll.201501284.

[39] Y. Min, K.C. Roche, S. Tian, M.J. Eblan, K.P. McKinnon, J.M. Caster, S. Chai, L. E. Herring, L. Zhang, T. Zhang, J.M. DeSimone, J.E. Tepper, B.G. Vincent, J. S. Serody, A.Z. Wang, Antigen-capturing nanoparticles improve the abscopal effect and cancer immunotherapy, Nat. Nanotechnol. 12 (9) (2017) 877–882, https://doi.org/10.1038/nnano.2017.113.

[40] M.S. Goldberg, Immunoengineering: how nanotechnology can enhance cancer immunotherapy, Cell 161 (2) (2015) 201–204, https://doi.org/10.1016/j.cell.2015.03.037.

[41] R. Wang, Z. He, P. Cai, Y. Zhao, L. Gao, W. Yang, Y. Zhao, X. Gao, F. Gao, Surface-functionalized modified copper sulfide nanoparticles enhance checkpoint blockade tumor immunotherapy by photothermal therapy and antigen capturing, ACS Appl. Mater. Interfaces 11 (15) (2019) 13964–13972, https://doi.org/10.1021/acsami.9b01107.

[42] X.P. Duan, C. Chan, W.B. Lin, Nanoparticle-mediated immunogenic cell death enables and potentiates cancer immunotherapy, Angew. Chem. Int. Ed. 58 (3) (2019) 670–680, https://doi.org/10.1002/anie.201804882.

[43] C. Song, H. Phuengkham, Y.S. Kim, V.V. Dinh, I. Lee, I.W. Shin, H.S. Shin, S.M. Jin, S.H. Um, H. Lee, K.S. Hong, S.-M. Jin, E. Lee, T.H. Kang, Y.-M. Park, Y.T. Lim, Syringeable immunotherapeutic nanogel reshapes tumor microenvironment and prevents tumor metastasis and recurrence, Nat. Commun. 10 (1) (2019) 3745, https://doi.org/10.1038/s41467-019-11730-8.

[44] G. Yang, L. Xu, Y. Chao, J. Xu, X. Sun, Y. Wu, R. Peng, Z. Liu, Hollow MnO2 as a tumor-microenvironment-responsive biodegradable nano-platform for combination therapy favoring antitumor immune responses, Nat. Commun. 8 (1) (2017) 902, https://doi.org/10.1038/s41467-017-01050-0.

[45] Y. Takahashi, N. Matsutani, T. Nakayama, H. Dejima, H. Uehara, M. Kawamura, Immunological effect of local ablation combined with immunotherapy on solid malignancies, Chin. J. Canc. 36 (1) (2017) 49, https://doi.org/10.1186/s40880-017-0216-5.

[46] Q. Liu, B. Zhai, W. Yang, L.X. Yu, W. Dong, Y.Q. He, L. Chen, L. Tang, Y. Lin, D. D. Huang, H.P. Wu, M.C. Wu, H.X. Yan, H.Y. Wang, Abrogation of local cancer recurrence after radiofrequency ablation by dendritic cell-based hyperthermic

[47] J. Lu, X. Liu, Y.-P. Liao, F. Salazar, B. Sun, W. Jiang, C.H. Chang, J. Jiang, X. Wang, A.M. Wu, H. Meng, A.E. Nel, Nano-enabled pancreas cancer immunotherapy using immunogenic cell death and reversing immunosuppression, Nat. Commun. 8 (1) (2017) 1811, https://doi.org/10.1038/s41467-017-01651-9.

[48] W. Song, L. Shen, Y. Wang, Q. Liu, T.J. Goodwin, J. Li, O. Dorosheva, T. Liu, R. Liu, L. Huang, Synergistic and low adverse effect cancer immunotherapy by immunogenic chemotherapy and locally expressed PD-L1 trap, Nat. Commun. 9 (1) (2018) 2237, https://doi.org/10.1038/s41467-018-04605-x.

[49] X. Tang, Q. Sheng, C. Xu, M. Li, J. Rao, X. Wang, Y. Long, Y. Tao, X. He, Z. Zhang, Q. He, pH/ATP cascade-responsive nano-courier with efficient tumor targeting and siRNA unloading for photothermal-immunotherapy, Nano Today 37 (2021), 101083, https://doi.org/10.1016/j.nantod.2021.101083.

[50] D.M. Pardoll, The blockade of immune checkpoints in cancer immunotherapy, Nat. Rev. Canc. 12 (4) (2012) 252–264, https://doi.org/10.1038/nrc3239.

[51] C. He, X. Duan, N. Guo, C. Chan, C. Poon, R.R. Weichselbaum, W. Lin, Core-shell nanoscale coordination polymers combine chemotherapy and photodynamic therapy to potentiate checkpoint blockade cancer immunotherapy, Nat. Commun. 7 (2016) 12499, https://doi.org/10.1038/ncomms12499.

[52] J. Yang, L. Hu, Immunomodulators targeting the PD-1/PD-L1 protein-protein interaction: from antibodies to small molecules, Med. Res. Rev. 39 (1) (2019) 265–301, https://doi.org/10.1002/med.21530.

[53] M. Konstantinidou, T. Zarganes-Tzitzikas, K. Magiera-Mularz, T.A. Holak, A. Domling, Immune checkpoint PD-1/PD-L1: is there life beyond antibodies? Angew. Chem. Int. Ed. 57 (18) (2018) 4840–4848, https://doi.org/10.1002/anie.201710407.

[54] R. Zhang, Z. Zhu, H. Lv, F. Li, S. Sun, J. Li, C.S. Lee, Immune checkpoint blockade mediated by a small-molecule nanoinhibitor targeting the PD-1/PD-L1 pathway synergizes with photodynamic therapy to elicit antitumor immunity and antimetastatic effects on breast cancer, Small 15 (49) (2019), e1903881, https://doi.org/10.1002/smll.201903881.

[55] H. Li, J.J. Li, W.D. Ke, Z.S. Ge, A near-infrared photothermal effect-responsive drug delivery system based on indocyanine green and doxorubicin-loaded polymeric micelles mediated by reversible diels-alder reaction, Macromol. Rapid Commun. 36 (20) (2015) 1841–1849, https://doi.org/10.1002/marc.201500337.

[56] S. Yamashita, H. Fukushima, Y. Akiyama, Y. Niidome, T. Mori, Y. Katayama, T. Niidome, Controlled-release system of single-stranded DNA triggered by the photothermal effect of gold nanorods and its in vivo application, Bioorg. Med. Chem. 19 (7) (2011) 2130–2135, https://doi.org/10.1016/j.bmc.2011.02.042.

[57] A.B. Bakhtiari, D. Hsiao, G. Jin, B.D. Gates, N.R. Branda, An efficient method based on the photothermal effect for the release of molecules from metal nanoparticle surfaces, Angew. Chem. Int. Ed. 48 (23) (2009) 4166–4169, https://doi.org/10.1002/anie.200805303.

[58] Y. Hu, L. Lin, J. Chen, A. Maruyama, H. Tian, X. Chen, Synergistic tumor immunological strategy by combining tumor nanovaccine with gene-mediated extracellular matrix scavenger, Biomaterials 252 (2020), 120114, https://doi.org/10.1016/j.biomaterials.2020.120114.

[59] T. Wang, D. Wang, H. Yu, B. Feng, F. Zhou, H. Zhang, L. Zhou, S. Jiao, Y. Li, A cancer vaccine-mediated postoperative immunotherapy for recurrent and metastatic tumors, Nat. Commun. 9 (1) (2018) 1532, https://doi.org/10.1038/s41467-018-03915-4.

[60] Y. Hu, L. Lin, J. Chen, K. Hao, S. Zhang, X. Guo, Z. Guo, H. Tian, X. Chen, Highly enhanced antitumor immunity by a three-barreled strategy of the l-arginine-promoted nanovaccine and gene-mediated PD-L1 blockade, ACS Appl. Mater. Interfaces 12 (37) (2020) 41127–41137, https://doi.org/10.1021/acsami.0c12734.

[61] Q. Chen, L. Xu, C. Liang, C. Wang, R. Peng, Z. Liu, Photothermal therapy with immune-adjuvant nanoparticles together with checkpoint blockade for effective cancer immunotherapy, Nat. Commun. 7 (1) (2016) 13193, https://doi.org/10.1038/ncomms13193.

[62] Y. Chen, R. Xia, Y. Huang, W. Zhao, J. Li, X. Zhang, P. Wang, R. Venkataramanan, J. Fan, W. Xie, X. Ma, B. Lu, S. Li, An immunostimulatory dual-functional nanocarrier that improves cancer immunochemotherapy, Nat. Commun. 7 (2016), https://doi.org/10.1038/ncomms13443.

[63] Q. Chen, M. Chen, Z. Liu, Local biomaterials-assisted cancer immunotherapy to trigger systemic antitumor responses, Chem. Soc. Rev. 48 (22) (2019) 5506–5526, https://doi.org/10.1039/c9cs00271e.

[64] M.S. Sabel, Cryo-immunology: a review of the literature and proposed mechanisms for stimulatory versus suppressive immune responses, Cryobiology 58 (1) (2009) 1–11, https://doi.org/10.1016/j.cryobiol.2008.10.126.

[65] X. Han, R. Wang, J. Xu, Q. Chen, C. Liang, J. Chen, J. Zhao, J. Chu, Q. Fan, E. Archibong, L. Jiang, C. Wang, Z. Liu, In situ thermal ablation of tumors in combination with nano-adjuvant and immune checkpoint blockade to inhibit cancer metastasis and recurrence, Biomaterials 224 (2019), 119490, https://doi.org/10.1016/j.biomaterials.2019.119490.

[66] S. Toraya-Brown, M.R. Sheen, P. Zhang, L. Chen, J.R. Baird, E. Demidenko, M. J. Turk, P.J. Hoopes, J.R. Conejo-Garcia, S. Fiering, Local hyperthermia treatment of tumors induces CD8(+) T cell-mediated resistance against distal and secondary tumors, Nanomed. Nanotechnol. 10 (6) (2014) 1273–1285, https://doi.org/10.1016/j.nano.2014.01.011.

[67] A.M. Watts, R.C. Kennedy, Quantitation of tumor foci in an experimental murine tumor model using computer-assisted video imaging, Anal. Biochem. 256 (2) (1998) 217–219, https://doi.org/10.1006/abio.1997.2497.

[68] S.K. Mishra, A.K. Srivastava, D. Kumar, R. Rajesh, Bio-functionalized Pt nanoparticles based electrochemical impedance immunosensor for human cardiac

myoglobin, RSC Adv. 4 (41) (2014) 21267–21276, https://doi.org/10.1039/c4ra00105b.

[69] S. Tanaka, J. Miyazaki, D.K. Tiwari, T. Jin, Y. Inouye, Fluorescent platinum nanoclusters: synthesis, purification, characterization, and application to bioimaging, Angew. Chem. Int. Ed. 123 (2) (2011) 451–455, https://doi.org/10.1002/ange.201004907.

[70] Q. Zhang, G. Kuang, S. He, H. Lu, Y. Cheng, D. Zhou, Y. Huang, Photoactivatable prodrug-backboned polymeric nanoparticles for efficient light-controlled gene delivery and synergistic treatment of platinum-resistant ovarian cancer, Nano Lett. 20 (5) (2020) 3039–3049, https://doi.org/10.1021/acs.nanolett.9b04981.

[71] J. Kim, Y.S. Bae, H. Lee, Shaped platinum nanoparticles directly synthesized inside mesoporous silica supports, Nanoscale 6 (21) (2014) 12540–12546, https://doi.org/10.1039/c4nr03951c.

[72] N. Tian, Z.Y. Zhou, S.G. Sun, Y. Ding, Z.L. Wang, Synthesis of tetrahexahedral platinum nanocrystals with high-index facets and high electro-oxidation activity, Science 316 (5825) (2007) 732–735, https://doi.org/10.1126/science.1140484.

[73] H. Yin, S. Zhao, K. Zhao, A. Muqsit, H. Tang, L. Chang, H. Zhao, Y. Gao, Z. Tang, Ultrathin platinum nanowires grown on single-layered nickel hydroxide with high hydrogen evolution activity, Nat. Commun. 6 (2015) 6430, https://doi.org/10.1038/ncomms7430.

[74] C.J. Yu, T.H. Chen, J.Y. Jiang, W.L. Tseng, Lysozyme-directed synthesis of platinum nanoclusters as a mimic oxidase, Nanoscale 6 (16) (2014) 9618–9624, https://doi.org/10.1039/c3nr06896j.

[75] T. Chen, T. Gu, L. Cheng, X. Li, G. Han, Z. Liu, Porous Pt nanoparticles loaded with doxorubicin to enable synergistic Chemo-/Electrodynamic Therapy, Biomaterials 255 (2020), 120202, https://doi.org/10.1016/j.biomaterials.2020.120202.

[76] X. Zheng, L. Wang, S. Liu, W. Zhang, F. Liu, Z. Xie, Nanoparticles of chlorin dimer with enhanced absorbance for photoacoustic imaging and phototherapy, Adv. Funct. Mater. 28 (26) (2018), 1706507, https://doi.org/10.1002/adfm.201706507.

[77] X. Zheng, L. Wang, M. Liu, P. Lei, F. Liu, Z. Xie, Nanoscale mixed-component metal–organic frameworks with photosensitizer spatial-arrangement-dependent photochemistry for multimodal-imaging-guided photothermal therapy, Chem. Mater. 30 (19) (2018) 6867–6876, https://doi.org/10.1021/acs.chemmater.8b03043.

[78] J. Zhang, C. Yang, R. Zhang, R. Chen, Z. Zhang, W. Zhang, S.H. Peng, X. Chen, G. Liu, C.S. Hsu, C.S. Lee, Biocompatible D-A semiconducting polymer nanoparticle with light-harvesting unit for highly effective photoacoustic imaging guided photothermal therapy, Adv. Funct. Mater. 27 (13) (2017), https://doi.org/10.1002/adfm.201605094.

[79] A. Gandini, The furan/maleimide Diels-Alder reaction: a versatile click-unclick tool in macromolecular synthesis, Prog. Polym. Sci. 38 (1) (2013) 1–29, https://doi.org/10.1016/j.progpolymsci.2012.04.002.

[80] Y. Ji, L. Zhang, X. Gu, W. Zhang, N. Zhou, Z. Zhang, X. Zhu, Sequence-controlled polymers with furan-protected maleimide as a latent monomer, Angew. Chem. Int. Ed. 56 (9) (2017) 2328–2333, https://doi.org/10.1002/anie.201610305.

[81] J.R. McElhanon, E.M. Russick, D.R. Wheeler, D.A. Loy, J.H. Aubert, Removable foams based on an epoxy resin incorporating reversible Diels–Alder adducts, J. Appl. Polym. Sci. 85 (7) (2002) 1496–1502, https://doi.org/10.1002/app.10753.

[82] X.F. Liu, H.B. Liu, W.D. Zhou, H.Y. Zheng, X.D. Yin, Y.L. Li, Y.B. Guo, M. Zhu, C.B. Ouyang, D.B. Zhu, A.D. Xia, Thermoreversible covalent self-assembly of oligo(p-phenylenevinylene) bridged gold nanoparticles, Langmuir 26 (5) (2010) 3179–3185, https://doi.org/10.1021/la903838w.

[83] J. Zhu, C. Waengler, R.B. Lennox, R. Schirrmacher, Preparation of water-soluble maleimide-functionalized 3 nm gold nanoparticles: a new bioconjugation template, Langmuir 28 (13) (2012) 5508–5512, https://doi.org/10.1021/la300316j.

[84] S. Yamashita, H. Fukushima, Y. Niidome, T. Mori, Y. Katayama, T. Niidome, Controlled-release system mediated by a retro diels-alder reaction induced by the photothermal effect of gold nanorods, Langmuir 27 (23) (2011) 14621–14626, https://doi.org/10.1021/la2036746.

[85] I.C. Kourtis, S. Hirosue, A. de Titta, S. Kontos, T. Stegmann, J.A. Hubbell, M.A. Swartz, Peripherally administered nanoparticles target monocytic myeloid cells, secondary lymphoid organs and tumors in mice, PloS One 8 (4) (2013), e61646, https://doi.org/10.1371/journal.pone.0061646.

[86] S.T. Reddy, A.J. van der Vlies, E. Simeoni, V. Angeli, G.J. Randolph, C.P. O'Neill, L.K. Lee, M.A. Swartz, J.A. Hubbell, Exploiting lymphatic transport and complement activation in nanoparticle vaccines, Nat. Biotechnol. 25 (10) (2007) 1159–1164, https://doi.org/10.1038/nbt1332.

[87] V. Manolova, A. Flace, M. Bauer, K. Schwarz, P. Saudan, M.F. Bachmann, Nanoparticles target distinct dendritic cell populations according to their size, Eur. J. Immunol. 38 (5) (2008) 1404–1413, https://doi.org/10.1002/eji.200737984.

[88] S. Liu, J. Yu, Q. Zhang, H. Lu, X. Qiu, D. Zhou, Y. Qi, Y. Huang, Dual cross-linked HHA hydrogel supplies and regulates MΦ2 for synergistic improvement of immunocompromise and impaired angiogenesis to enhance diabetic chronic wound healing, Biomacromolecules 21 (9) (2020) 3795–3806, https://doi.org/10.1021/acs.biomac.0c00891.

[89] S. Liu, Q. Zhang, J. Yu, N. Shao, H. Lu, J. Guo, X. Qiu, D. Zhou, Y. Huang, Absorbable thioether grafted hyaluronic acid nanofibrous hydrogel for synergistic modulation of inflammation microenvironment to accelerate chronic diabetic wound healing, Adv. Healthc. Mater. 9 (11) (2020), 2000198, https://doi.org/10.1002/adhm.202000198.

[90] L. Fend, T. Yamazaki, C. Remy, C. Fahrner, M. Gantzer, V. Nourtier, X. Preville, E. Quemeneur, O. Kepp, J. Adam, A. Marabelle, J.M. Pitt, G. Kroemer, L. Zitvogel, Immune checkpoint blockade, immunogenic chemotherapy or IFN-alpha blockade boost the local and abscopal effects of oncolytic virotherapy, Cancer Res. 77 (15) (2017) 4146–4157, https://doi.org/10.1158/0008-5472.can-16-2165.

[91] K. Guzik, K.M. Zak, P. Grudnik, K. Magiera, B. Musielak, R. Torner, L. Skalniak, A. Domling, G. Dubin, T.A. Holak, Small-molecule inhibitors of the programmed cell death-1/programmed death-ligand 1 (PD-1/PD-L1) interaction via transiently induced protein states and dimerization of PD-L1, J. Med. Chem. 60 (13) (2017) 5857–5867, https://doi.org/10.1021/acs.jmedchem.7b00293.

[92] L. Skalniak, K.M. Zak, K. Guzik, K. Magiera, B. Musielak, M. Pachota, B. Szelazek, J. Kocik, P. Grudnik, M. Tomala, S. Krzanik, K. Pyrc, A. Domling, G. Dubin, T.A. Holak, Small-molecule inhibitors of PD-1/PD-L1 immune checkpoint alleviate the PD-L1-induced exhaustion of T-cells, Oncotarget 8 (42) (2017) 72167–72181, https://doi.org/10.18632/oncotarget.20050.

[93] S.M. Kaech, E.J. Wherry, R. Ahmed, Effector and memory T-cell differentiation: implications for vaccine development, Nat. Rev. Immunol. 2 (4) (2002) 251–262, https://doi.org/10.1038/nri778.

[94] E.J. Wherry, V. Teichgraber, T.C. Becker, D. Masopust, S.M. Kaech, R. Antia, U.H. von Andrian, R. Ahmed, Lineage relationship and protective immunity of memory CD8 T cell subsets, Nat. Immunol. 4 (3) (2003) 225–234, https://doi.org/10.1038/ni889.

[95] Z. Zhang, G. Kuang, S. Zong, S. Liu, H. Xiao, X. Chen, D. Zhou, Y. Huang, Sandwich-like fibers/sponge composite combining chemotherapy and hemostasis for efficient postoperative prevention of tumor recurrence and metastasis, Adv. Mater. 30 (49) (2018) 9, https://doi.org/10.1002/adma.201803217.